Minimal port-Hamiltonian modeling of voice production: choices of fluid flow hypotheses, resulting structure and comparison

Thomas Risse, Thomas Hélie, Fabrice Silva, Antoine Falaize

Minimal port-Hamiltonian modeling of voice production: choices of fluid flow hypotheses, resulting structure and comparison

Thomas Risse * **Thomas Hélie** * **Fabrice Silva** **
Antoine Falaize ***

* *IRCAM, Paris, France (e-mail: thomas.risse@ircam.fr, thomas.helie@ircam.fr).*
** *Aix Marseille Univ, CNRS, Centrale Marseille, LMA UMR 7031, Marseille, France(e-mail: silva@lma.cnrs-mrs.fr)*
*** *LaSIE, La Rochelle, France (e-mail: antoine.falaize@univ-lr.fr)*

Abstract: Voice production results from the interaction between expelled airflow and soft tissues in the larynx and the vocal tract. Among the large literature on this topic over the last fifty years, a few nonlinear fluid-structure interaction models have been proposed in the port-Hamiltonian framework for passivity purposes. In this paper, we examine, compare and discuss two lumped-element port-Hamiltonian models from the literature, both derived from distributed parameter descriptions and simplifying assumptions chosen to integrate the minimal relevant phenomena involved in the larynx (for self-oscillations) or the vocal tract (during articulation). These models are recalled and reformulated using common terminology and notations. This leads to equivalent circuit representations, the components and the structure of which allow direct comparison (about causality, dimension, nonlinear laws, coupling) and physical interpretation. These results highlight important properties to consider and provide guidelines for future modelling improvement to be used in simulation.

Keywords: Modelling, Port-Hamiltonian systems, Distributed parameter systems, Fluid-structure interaction, Vocal apparatus

1. INTRODUCTION

A number of classical 1D lumped-element models (Ishizaka and Flanagan (1972), Story and Titze (1994)) of the larynx are built considering that the glottal flow is incompressible, quasi-steady (negligible inertial forces), in a quasi-static domain (negligible fluid transverse velocity). These assumptions allow the derivation of the flow equation using modified Bernoulli laws. They have been discussed theoretically and tested experimentally by a number of authors for different vocal folds geometries and frequency ranges (see Wang et al. (2023) and the many studies of Hirshberg, Pelorson and van Hirtum [1]). These assumptions appear to be mostly valid, only provided that the larynx is not acoustically loaded by a vocal tract and vibrates at a low frequency.

Models accounting for fluid inertia and structure induced flow are mostly based on fluid flow solvers of high dimensions (e.g. De Vries et al. (2002)). For the last 10 years, efforts have been made in the port-Hamiltonian (pH) formalism to develop low dimensional power-balanced models of the glottal flow and more generally of the vocal apparatus. First, Encina et al. (2015) proposed a pH model of the vocal folds based on the so-called *body-cover model* of Story and Titze (1994). Hélie and Silva (2017) developed a first self-oscillating assembly, which incorporates an incompressible flow between two parallel moving plates and considers the power exchange at fluid-structure interfaces (extending the work of Lopes and Hélie (2016)). Mora et al. (2018) proposed a lumped incompressible fluid flow model for connection to the mechanical part of the *body-cover model*. However, their approach is not scalable.

More recently, Mora et al. (2021b) and Wetzel (2021) proposed two *scalable* power-balanced lumped-element models for *compressible fluid* in tube with moving boundaries, aimed at voice production modeling. This paper aims to examine, compare and discuss these models, highlighting relevant properties (model dimension, input causality, nature of the exchanged power at Fluid-Structure interfaces) and providing guidelines for future model improvement.

The paper is structured as follows. Section 2 reviews the general setting (geometry, starting fluid equations) and hypotheses common to both models. Sections 3 and 4 respectively detail the pH models proposed by Mora et al. (2021b) and by Wetzel (2021). To prepare comparison, a particular attention is paid to consider energy variables (and so, flows/effort) of the same nature for both models, chosen to yield canonical Dirac structures. Both models are presented in the form of equivalent electrical circuits. These resulting structures allows direct comparison and interpretation, leading to discussion in section 5. Section 6 concludes this discussion with guidelines for improving future models to be used in simulation.

[1] see e.g. Ruty et al. (2007).

2. GENERAL SETTING

Both approaches in Mora et al. (2021b) and Wetzel (2021) aim at proposing simplified pH descriptions of a compressible fluid in a pipe with time-varying cross sections.

The time-varying domain $\Omega(t)$ is composed of segments with same length l_0, each of them having time varying height $h_j(t)$ and volume $V_j(h_j) = S_0\, h_j$, $j = 1, \dots, N$, where S_0 denotes the area of the (upper) fluid-structure interface (see Fig. 1). Note that, as detailed below, Mora *et al.* additionally introduce interleaved domains and half-segments built on the geometry of Fig. 1 (see Fig. 2).

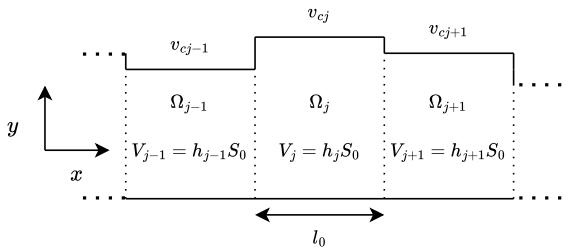

Fig. 1. (Time-varying) geometry parametrisation.

The domain $\Omega(t)$ is occupied by a compressible, isentropic, viscous fluid in irrotational flow. The associated governing equations are [2] :

$$\frac{\partial \rho}{\partial t} = -div\,(\rho \boldsymbol{v}), \tag{1a}$$

$$\frac{\partial \boldsymbol{v}}{\partial t} = -\boldsymbol{grad}\left(\frac{1}{2}|\boldsymbol{v}|^2\right) - \frac{1}{\rho}\boldsymbol{grad}\, p - \frac{1}{\rho} div\, \tau, \tag{1b}$$

with ρ the fluid density, $\boldsymbol{v}$ the fluid velocity, p the thermodynamic pressure and τ the viscosity tensor. The system is closed by defining the fluid specific internal energy density $u(\rho)$. The total energy is given by

$$E(t) = \int_{\Omega(t)} \left(\frac{1}{2}\rho(\boldsymbol{r},t)\boldsymbol{v}(\boldsymbol{r},t)^2 + \rho(\boldsymbol{r},t)\, u\big(\rho(\boldsymbol{r},t)\big)\right) \mathrm{d}\Omega(\boldsymbol{r}). \tag{2}$$

Both models use (1) as a basis to derive quasi-1D systems.

3. FLUID MODEL OF Mora et al. (2021b)

3.1 Original model description

The model uses a staggered grid finite difference discretisation (see Trenchant et al. (2018)) of the axial velocity and density averaged over a cross section. The dynamics of the transverse velocity is ignored. For these choices, the dynamics appears to be governed by a 1D PDE system.

The chosen state variables are [3] $\boldsymbol{x}^o = [\boldsymbol{v}^\intercal, \widetilde{\boldsymbol{\rho}}^\intercal]$, with $\boldsymbol{v} = [v_1, .., v_N]^\intercal$ the mean axial velocities in domains $\Omega_j(t)$ of volume $V_j(h_j)$ and $\widetilde{\boldsymbol{\rho}} = [\widetilde{\rho}_1, \dots, \widetilde{\rho}_{N-1}]^\intercal$ the mean densities in the corresponding staggered domains $\widetilde{\Omega}_j(t)$ of volume $\widetilde{V}_j(h_{j-1}, h_j)$, see Fig. 2. While a geometry state is needed to write the Hamiltonian of the system, in Mora et al. (2021b) it is chosen to deduce this state from the tissue configuration once the connected model is built. For comparison purposes and for completeness of the stand-alone fluid system, we choose to add back $\boldsymbol{h} = [h_i, h_1, .., h_N]^\intercal$, the heights of duct segments to the state, leading to the new state

$$\boldsymbol{x}^o_h = [\boldsymbol{v}^\intercal, \widetilde{\boldsymbol{\rho}}^\intercal, \boldsymbol{h}^\intercal]. \tag{3}$$

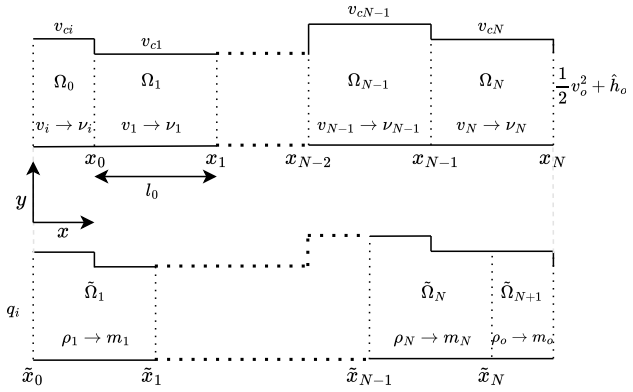

Fig. 2. Mora's model spatial discretisation of fluid variables for original and modified state. Recall that the division into segments $\Omega_j(t)$ (top) is related to an average velocity and $\widetilde{\Omega}_j(t)$ (down) to an average mass density.

Finally, the control causality at the duct extremities can be changed by using half segments. Here, we stick to the configuration chosen by Mora et al. (2021b): a half-segment at left and a full segment at right. The resulting pH system admits the following inputs and outputs :

$$\boldsymbol{u}^o = [\psi_o, q_i, \boldsymbol{v}_c^\intercal]^\intercal, \qquad \text{(input)} \tag{4a}$$

$$\boldsymbol{y}^o = [-q_o, -\psi_i, -\boldsymbol{F}_c^\intercal]^\intercal, \qquad \text{(output)} \tag{4b}$$

which embeds the set of contact surfaces velocities $\boldsymbol{v}_c = [v_{ci}, v_{c1}, .., v_{cN}]^\intercal$ and forces $\boldsymbol{F}_c = [F_{ci}, F_{c1}, ..., F_{cN}]^\intercal$, the upstream mass flow q_i (at $x = \widetilde{x}_0$) and enthalpy ψ_i and the downstream total enthalpy ψ_o (at $x = x_N$) and mass flow q_o, as represented in Fig. 2.

3.2 Modified model using a change of variable

The pH models based either on $\boldsymbol{x}^o$ or on $\boldsymbol{x}^o_h$ appear to have an interconnection modulated by the state variables. To ease comparison and interpretation, we propose the following change of state that restores a canonical structure:

$$(v_j, \widetilde{\rho}_j, h_j) \to (\nu_j, \widetilde{m}_j, h_j) \text{ for } j \in [1, N], \tag{5}$$

with $\nu_j = l_0 v_j$ and $\widetilde{m}_j = \widetilde{\rho}_j \widetilde{V}_j(h_{j-1}, h_j)$ the fluid mass within $\widetilde{\Omega}_j(t)$. Additionally, we define the corresponding quantities $\nu_i = \frac{l_0}{2} v_i$ and $\widetilde{m}_o = \widetilde{\rho}_o \frac{V_N(h_N)}{2}$ at the boundaries. Using the modified state

$$\boldsymbol{x}^m = [\nu_i, \boldsymbol{\nu}^\intercal, \widetilde{\boldsymbol{m}}^\intercal, \widetilde{m}_o, \boldsymbol{h}^\intercal]^\intercal, \tag{6a}$$

the Hamiltonian writes

$$H^m(\boldsymbol{x}^m) = H_k(\boldsymbol{x}^m) + H_p(\widetilde{\boldsymbol{m}}, \boldsymbol{h}, \widetilde{m}_o), \tag{6b}$$

with kinetic energy

$$H_k(\boldsymbol{x}^m) = \sum_{j=1}^{N-1} \frac{1}{2l_0^2} h_j \left(\frac{\widetilde{m}_j}{h_{j-1} + h_j} + \frac{\widetilde{m}_{j+1}}{h_j + h_{j+1}}\right) \nu_j^2 + \frac{1}{2}\widetilde{m}_1 \frac{V_0}{\widetilde{V}_1} \left(\frac{\nu_i}{2l_0}\right)^2 + \frac{1}{2l_0^2}\left(\frac{h_N \widetilde{m}_N}{h_{N-1} + h_N} + \widetilde{m}_o\right) \nu_N^2, \tag{6c}$$

[2] For a port-Hamiltonian description of infinite dimensional fluid equations, see Mora et al. (2021a).

[3] The superscript o in $\boldsymbol{x}^o$ and other variables accounts for "original model", with the notations used in Mora et al. (2021b).

and potential energy

$$H_p(\widetilde{\boldsymbol{m}}, \boldsymbol{h}, m_o) = \sum_{j=1}^{N} \widetilde{m}_j \, u(\widetilde{\rho}_j) + \widetilde{m}_o \, u(\widetilde{\rho}_o), \tag{6d}$$

where $\widetilde{\rho}_j : (\widetilde{\boldsymbol{m}}, \boldsymbol{h}) \mapsto \widetilde{\rho}_j(\widetilde{\boldsymbol{m}}, \boldsymbol{h}) = \dfrac{\widetilde{m}_j}{\widetilde{V}_j(h_{j-1}, h_j)}$ gives the mean density in the domain $\widetilde{\Omega}_j(t)$.

Remark 1. (variables ν_i, ρ_o). The total energy depends on variables ν_i and m_o defined at extremities. In the following, we include these variables in the state to consider their associated efforts and flows inside the end half-segments, while the original work consider them as input variables in the power balance (Mora et al., 2021b, equation (3.34)). Note that for the interpretation into equivalent electric circuit in Table 1, we will focus only on the internal segments, which are not impacted by this choice. However, this modification reverses the causality of the control at the open boundaries.

From this definitions, we can derive and identify the associated efforts $\nabla H^m(\boldsymbol{x}^m)$. Gradient with respect to ν_j regenerates the mean mass flow q_j in $\Omega_j(t)$, considered equal to the mass flow at point $\widetilde{x}_j$

$$\begin{aligned} \partial_{\nu_j} H^m &= \frac{1}{l_0^2} h_j \left(\frac{\widetilde{m}_j}{h_{j-1}+h_j} + \frac{\widetilde{m}_{j+1}}{h_j + h_{j+1}} \right) \nu_j \\ &= L_0 h_j \left(\frac{\widetilde{\rho}_j + \widetilde{\rho}_{j+1}}{2} \right) v_j \\ &= q_j(\boldsymbol{x}^m) = q_{|\widetilde{x}_j}(\boldsymbol{x}). \end{aligned} \tag{7a}$$

Gradient with respect to $\widetilde{m}_j$ is

$$\begin{aligned} \partial_{\tilde{m}_j} H^m &= \frac{1}{2l_0^2} \left(\frac{h_{j-1}\nu_{j-1}^2 + h_j \nu_j^2}{h_{j-1}+h_j} \right) \\ &\quad + \underbrace{u(\widetilde{\rho}_j) + \widetilde{\rho}_j u'(\widetilde{\rho}_j)}_{\widetilde{e}_j(\boldsymbol{x})} \\ &= \widetilde{\psi_j}(\boldsymbol{x}), \end{aligned} \tag{7b}$$

with $\widetilde{e}_j(\boldsymbol{x})$ the mean specific enthalpy in $\widetilde{\Omega}_j(t)$ and $\widetilde{\psi}_j(\boldsymbol{x})$ the mean total enthalpy in $\widetilde{\Omega}_j(t)$. Finally, the gradient with respect to h_j regenerates the effective force F_{cj} received by the fluid at the contact surface of $\Omega_j(t)$

$$\begin{aligned} \partial_{h_j} H^m &= -\, l_0 L_0 \left(\frac{\widetilde{\rho}_j^2 u'(\widetilde{\rho}_j) + \widetilde{\rho}_{j+1}^2 u'(\widetilde{\rho}_{j+1})}{2} \right) \\ &\quad - \frac{l_0 L_0}{4} \left(\widetilde{\rho}_j \widetilde{v}_j^2 + \widetilde{\rho}_{j+1} \widetilde{v}_{j+1}^2 - \frac{(\widetilde{\rho}_j + \widetilde{\rho}_{j+1}) \nu_j^2}{l_0^2} \right) \\ &= F_{cj}, \end{aligned} \tag{7c}$$

introducing function $\widetilde{v}_j^2 : (\boldsymbol{h}, \boldsymbol{\nu}) \mapsto \dfrac{h_{j-1}(\frac{\nu_{j-1}}{l_0})^2 + h_j(\frac{\nu_j}{l_0})^2}{h_{j-1}+h_j}$ that evaluates the average squared velocity on $\widetilde{\Omega}_j(t)$.

From these definitions, we get the following modified system of equations for the inner segments :

$$\dot{\nu}_j = \partial_{\tilde{m}_j} H^m - \partial_{\tilde{m}_{j+1}} H^m - \phi_j, \tag{8}$$

$$\dot{\widetilde{m}}_j = \partial_{\nu_{j-1}} H^m - \partial_{\nu_j} H^m, \tag{9}$$

$$\dot{h}_j = v_{cj}, \tag{10}$$

where $\phi_j : (\boldsymbol{x}^m) \mapsto \phi_j(\boldsymbol{x}^m)$ gives the average velocity drop due to energy losses in the j-th velocity section, defined as in the original publication. Finally, at the left-hand side of the duct we have

$$\dot{\nu}_i = \psi_i - \partial_{\tilde{m}_1} H^m - \phi_i, \tag{11}$$

and at the right-hand side

$$\dot{m}_o = \partial_{\nu_N} H^m - q_o. \tag{12}$$

Using state $\boldsymbol{x}^m$ and input/output variables $\boldsymbol{u}^m = [\psi_i, q_0, \boldsymbol{v}_c^\intercal]$, $\boldsymbol{y}^m = [-q_i, -\psi_o, -\boldsymbol{F}_c^\intercal]$, the following modified dissipative port-Hamiltonian system can finally be built

$$\dot{\boldsymbol{x}}^m = [J^m - R^m(\boldsymbol{x}^m)] \nabla H^m(\boldsymbol{x}^m) + G^m \boldsymbol{u}^m, \tag{13}$$

$$\boldsymbol{y}^m = -G^{m\intercal} \nabla H^m(\boldsymbol{x}^m). \tag{14}$$

The system matrices are

$$\begin{aligned} J^m &= \begin{bmatrix} \mathbf{0} & V & \mathbf{0} \\ -V^\intercal & \mathbf{0} & \mathbf{0} \\ \mathbf{0} & \mathbf{0} & \mathbf{0} \end{bmatrix}, \quad G^m = \begin{bmatrix} -g_\nu & \mathbf{0} & \mathbf{0} \\ \mathbf{0} & g_m & \mathbf{0} \\ \mathbf{0} & \mathbf{0} & \mathbb{I}_{N+1} \end{bmatrix}, \\ R^m(\boldsymbol{x}^m) &= \begin{bmatrix} R_\nu(\boldsymbol{x}^m) & \mathbf{0} & \mathbf{0} \\ \mathbf{0} & \mathbf{0} & \mathbf{0} \\ \mathbf{0} & \mathbf{0} & \mathbf{0} \end{bmatrix}, \end{aligned} \tag{15}$$

with

$$V = \begin{bmatrix} -1 & 0 & \cdots & \cdots & \cdots & 0 \\ 1 & -1 & 0 & & & \vdots \\ \vdots & \ddots & \ddots & & & \vdots \\ \vdots & & \ddots & \ddots & & \vdots \\ \vdots & & & 1 & -1 & 0 \\ 0 & \cdots & \cdots & \cdots & 1 & -1 \end{bmatrix}, g_\nu = \begin{bmatrix} 1 \\ 0 \\ \vdots \\ 0 \end{bmatrix}, \quad g_m = \begin{bmatrix} 0 \\ \vdots \\ 0 \\ 1 \end{bmatrix}, \tag{16}$$

$$R_\nu(\boldsymbol{x}^m) = l_0^2 \begin{bmatrix} d_{fj}(\boldsymbol{x}^m) & \cdots & 0 \\ \vdots & \ddots & \vdots \\ 0 & \cdots & d_{fn}(\boldsymbol{x}^m) \end{bmatrix}. \tag{17}$$

Functions d_{fj} are defined in Mora et al. (2021b), page 11.

3.3 Equivalent electrical circuit

The reformulated model with a canonical matrix J is used to construct a simple equivalent electronic circuit [4] of a single segment of Mora et al. (2021b) fluid model, as shown in table 1.a. This circuit highlights the connections between the lumped elements of the system and clearly exhibits two sub-circuits. The first has the structure of a classical transmission line, which is found e.g. in modeling of acoustic waves in tubes with time independent geometry. The second sub-circuit encodes geometry variations and fluid structure interaction.

Although the two sub-circuits are not structurally related, they are in fact coupled by the not-separable Hamiltonian $H^m(\boldsymbol{x}^m)$ defined by (6b). While the equivalent circuit representation allows to identify a common structure, the Hamiltonian makes it dependent on the chosen state vector. In fact, using the original state $\boldsymbol{x}^o$, the equivalent circuit is modified so that both sub-circuits are structurally coupled through a transformer.

[4] The convention used is to represent mass flows and contact surface velocities as currents, and total specific enthalpy and forces as potentials.

4. FLUID MODEL OF Wetzel (2021)

Wetzel's model is built using a different approach : a first dynamical system is derived for a single fluid cell as shown Fig. 3. Several of these cells are then used as building blocks and connected together to form the full model.

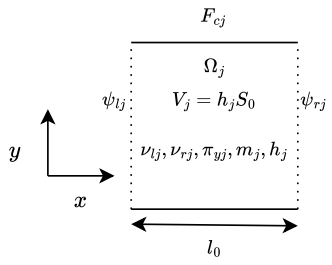

Fig. 3. Single fluid cell of Wetzel's model

4.1 Single fluid cell

In each cell $\Omega_j(t)$, the fluid is described by its mean density and by a three d.o.f approximation of the velocity field. The axial velocity field is considered linear with coordinate x and independent of y. The transverse velocity field is linear with y and independent of x. The dynamics of each macroscopic field can be derived by injecting these fields into the conservation equations (1) and integrating them. Wetzel's thesis provides a set of state variables

$$\boldsymbol{x}_j = [\nu_{lj}, \nu_{rj}, \pi_{yj}, m_j, h_j]^\intercal, \tag{18}$$

leading to a canonical representation of the dynamics in the fluid cell. ν_{lj} and ν_{rj} are axial kinematic variables, π_{yj} is a transverse kinematic variable, m_j is the mass of fluid in the cell and h_j the height of the cell. For more details about definitions of the kinematic variables, refer to (Wetzel, 2021, chapter 3).The Hamiltonian of the fluid cell is

$$\begin{aligned} H_j(\boldsymbol{x}_j) =& \underbrace{\frac{2m}{l_0^2}(\nu_{lj}^2 + \nu_{rj}^2 - \nu_{lj}\nu_{rj})}_{\text{axial kinetic}} \\ &+ \underbrace{\frac{3\pi_{yj}^2}{2m_j}}_{\text{transverse kinetic}} + \underbrace{m_j u\left(\frac{m_j}{S_0 h_j}\right)}_{\text{internal/potential}}, \end{aligned} \tag{19}$$

where $u(\rho)$ is the chosen internal energy density. By design of $\boldsymbol{x}_j$, the effort vector reads

$$\nabla H_j(\boldsymbol{x}_j) = \begin{bmatrix} \partial_{\nu_{lj}} H_j = q_{lj} \\ \partial_{\nu_{rj}} H_j = q_{rj} \\ \partial_{\pi_{yj}} H_j = v_{cj} \\ \partial_{\nu_{mj}} H_j = \psi_j \\ \partial_{\nu_{hj}} H_j = -p_j S_0 \end{bmatrix}, \tag{20}$$

with q_l the mass flow at the left interface, q_r the mass flow at the right interface, $v_{cj} = \dot{h}_j$ the fluid-structure interface velocity, ψ_j the volume-averaged total specific enthalpy and p_j the volume-averaged thermodynamic pressure.

Using $\boldsymbol{u}_j = [\psi_{lj}, \psi_{rj}, F_{cj}]^\intercal$ as input vector, with ψ_{lj} the total specific enthalpy at the left interface, ψ_{rj} total specific enthalpy at the left interface and F_{cj} the force applied by the structure on the fluid, the port-Hamiltonian formulation reads

$$\begin{bmatrix} \dot{\boldsymbol{x}}_j \\ \boldsymbol{w}_j \\ -\boldsymbol{y}_j \end{bmatrix} = \begin{bmatrix} A_0 & B_0 & G_0 \\ -B_0^\intercal & \mathbf{0} & \mathbf{0} \\ -G_0^\intercal & \mathbf{0} & \mathbf{0} \end{bmatrix} \begin{bmatrix} \nabla H_j(\boldsymbol{x}_j) \\ \boldsymbol{z}_j(\boldsymbol{w}_j, \boldsymbol{x}_j) \\ \boldsymbol{u}_j \end{bmatrix}, \tag{21}$$

with $\boldsymbol{y}_j = [-q_{lj}, q_{rj}, -v_{cj}]$ the associated output vector.

Interconnection matrices are

$$A_0 = \begin{bmatrix} 0 & 0 & 0 & -1 & 0 \\ 0 & 0 & 0 & 1 & 0 \\ 0 & 0 & 0 & 0 & -1 \\ 1 & -1 & 0 & 0 & 0 \\ 0 & 0 & 1 & 0 & 0 \end{bmatrix}, B_0 = \begin{bmatrix} -1 & 0 \\ 0 & 1 \\ 0 & -1 \\ 0 & 0 \\ 0 & 0 \end{bmatrix}, G_0 = \begin{bmatrix} 1 & 0 & 0 \\ 0 & -1 & 0 \\ 0 & 0 & 1 \\ 0 & 0 & 0 \\ 0 & 0 & 0 \end{bmatrix}. \tag{22}$$

Note that $\boldsymbol{w}_j \equiv [\dot{m}_j, v_{cj}]^\intercal$ and the associated laws

$$\boldsymbol{z}_j(\boldsymbol{w}_j, \boldsymbol{x}_j) = \left[v_{cj}\frac{\pi_{yj}}{m_j}, -\frac{\pi_{yj}}{m_j}\dot{m}_j \right]^\intercal, \tag{23}$$

form a conservative gyrator, modulating the efforts by $\frac{\pi_{yj}}{m_j}$. They are necessary to obtain a canonical interconnection matrix.

4.2 Assembled fluid system

Assembly of the full fluid domain is done by imposing mass flow continuity at interfaces between individual cells. This condition writes

$$q_{rj-1} = q_{lj}. \tag{24}$$

As both q_{rj-1} and q_{lj} are outputs of the cell's pH representation, the condition transcribes as effort constraints on the assembled pH system.

The full state

$$\boldsymbol{x}_f = [\boldsymbol{\nu}_l^\intercal, \boldsymbol{\nu}_r^\intercal, \boldsymbol{\pi}_y^\intercal, \boldsymbol{m}^\intercal, \boldsymbol{h}^\intercal]^\intercal, \tag{25}$$

is defined, with

$$\begin{aligned} \boldsymbol{\nu}_l = [\nu_{l1}, .., \nu_{lN}]^\intercal, \quad \boldsymbol{\nu}_r = [\nu_{r1}, .., \nu_{rN}]^\intercal, \\ \boldsymbol{\pi}_y = [\pi_{y1}, .., \pi_{yN}]^\intercal, \quad \boldsymbol{m} = [m_1, .., m_N]^\intercal, \\ \boldsymbol{h} = [h_1, .., h_N]^\intercal. \end{aligned} \tag{26}$$

Using the same procedure, the vector $\boldsymbol{w}_f = [\dot{\boldsymbol{m}}^\intercal, \boldsymbol{v}_c]$ and corresponding function $\boldsymbol{z}_f(\boldsymbol{w}_f, \boldsymbol{x}_f)$, as well as the complete input $\boldsymbol{u}_f = [\psi_{l0}, \psi_{rN}, \boldsymbol{F}_c]^\intercal$ and output $\boldsymbol{y}_f = [-q_{l1}, q_{rN}, -\boldsymbol{v}_c]^\intercal$ vectors are built. The Hamiltonian associated with the assembly reads

$$H_f(\boldsymbol{x}_f) = \sum_{j=1}^{N} H_j(\boldsymbol{x}_j). \tag{27}$$

Finally, the assembled pH model is

$$\begin{bmatrix} \dot{\boldsymbol{x}}_f \\ \boldsymbol{w}_f \\ \mathbf{0} \\ -\boldsymbol{y}_f \end{bmatrix} = \begin{bmatrix} A & B & -C^\intercal & G \\ -B^\intercal & \mathbf{0} & \mathbf{0} & \mathbf{0} \\ C & \mathbf{0} & \mathbf{0} & \mathbf{0} \\ -G^\intercal & \mathbf{0} & \mathbf{0} & \mathbf{0} \end{bmatrix} \begin{bmatrix} \nabla H_f(\boldsymbol{x}_f) \\ \boldsymbol{z}_f(\boldsymbol{w}_f, \boldsymbol{x}_f) \\ \boldsymbol{\lambda}_f \\ \boldsymbol{u}_f \end{bmatrix}, \tag{28}$$

with $\boldsymbol{y}_f = [-q_{l0}, q_{rN}, -\boldsymbol{v}_c]^\intercal$ the full output vector and where $\boldsymbol{\lambda}_f$ is a set of Lagrange multipliers related to constraints equations (24). Matrices A and B are respectively given by expressions for A_0 and B_0 in equation (22),

replacing the scalar 0 by matrices of zeros $\mathbf{0}_{N,N}$ and the scalar 1 by identity matrices $\mathbb{I}_N$. The matrix C given by

$$C = [\mathbf{0}_{N-1,1}\ \mathbb{I}_{N-1}\ -\mathbb{I}_{N-1}\ \mathbf{0}_{N-1,1}\ \mathbf{0}_{N-1,3N}], \quad (29)$$

encodes the $N-1$ constraints equations and matrix G is given by

$$G = \begin{bmatrix} [1,0,..,0] & \mathbf{0}_{1,N} & \mathbf{0}_{1,N} & \mathbf{0}_{1,N} & \mathbf{0}_{1,N} \\ \mathbf{0}_{1,N} & [0,..,0,-1] & \mathbf{0}_{1,N} & \mathbf{0}_{1,N} & \mathbf{0}_{1,N} \\ \mathbf{0}_{N,N} & \mathbf{0}_{N,N} & \mathbb{I}_N & \mathbf{0}_{N,N} & \mathbf{0}_{N,N} \end{bmatrix}^\intercal . \quad (30)$$

Note that the fluid system is fully conservative. Wetzel (2021) proposed to add lumped dissipation between each segments when building the assembled system, which we omitted here for simplicity.

4.3 Equivalent electrical circuit

Table 1.b shows the equivalent circuit of a single cell of Wetzel (2021)'s model. It exhibits a transmission line structure on the axial velocity dynamics coupled with the transverse flow through a gyrator. The assembly of multiple cells leads to (electrical) masses of state ν_{rj-1} and ν_{lj} connected in series, responsible for the constraint equations. Note that one could pre-solve the constraints thus building equivalent masses at each junctions. However, and because of the coupling between ν_{lj} and ν_{rj} in the Hamiltonian of a single cell, this process is not straightforward for the connection of more than two cells. Moreover, it would result in a modified dense interconnection matrix, making the structural analysis difficult.

5. COMPARISON AND DISCUSSION

5.1 Fluid systems structural comparison

In summary, both models have a similar structure that corresponds to axial velocity and mass accumulation. This structure takes the form of a canonical transmission line when the state is chosen so that the efforts are mass flows and enthalpy. When focusing on a segment, Mora's axial structure has a Π shape while Wetzel's axial structure has a T shape. This difference is due to the choice of discretisation: in the first case, masses are defined at junctions and velocities in the segments whereas in the second case, the opposite choice is made.

The addition of a transverse velocity component π_{yj} in Wetzel's model induces a change in input causality at the fluid-structure interface from velocity-controlled to force-controlled and results in structural coupling between the axial dynamics and the fluid-structure interface. Note that the fluid-structure coupling force f_{cj} of both models deserves a detailed physical interpretation or numerical investigation to understand and quantify the role played by the transverse velocity component of Wetzel's model. As a first step, note that the cancellation of this transverse component (by imposing $\pi_{yj} = 0$, $\dot{\pi}_{yj} = 0$ in the dynamics of (21)) causes a constraint to appear instead of $\partial_{\pi_{yj}} H_j$ and removes the gyrator of coefficient $-\frac{\pi_{yj}}{m_j}$. However, this constraint is naturally solved by choosing the same generator as in the Mora's circuit (velocity source). This results in the same decoupled structure as Mora's circuit, which then interprets as an asymptotic case ($\pi_{yj} \to 0$) of Wetzel's coupling. At the same time, this modification reduces the number of dof in the model to 3N.

5.2 Connection to deformable tissues

Both work use simple lumped parameters representations of the tissues built as assemblies of spring, damper and masses. The fundamental difference comes form the causality of the fluid-structure connection. Mora's fluid model accepts a causal connection with masses-like components while Wetzel's model is causal when connected to spring-like components. Classical vocal folds model such as the body-cover model from Story and Titze (1994) (interpreted as a pH system in Encina et al. (2015)), present masses at the fluid-structure interface thus making them easier to connect to Mora's model. It should be noted that Mora proposed to connect multiple fluid sections to single solid masses. This allows an arbitrary spatial resolution for the fluid, independent of the chosen tissue model complexity.

Both models become ill-conditioned when approaching contact, as division by h_j occurs in the dynamic equations and stiffen the equations on $\dot{h}_j$. Mora proposes a method for handling contact during simulation. It consists of disconnecting the fluid from the structure and resetting the fluid state when the height h_j of a segment becomes smaller than a threshold. Contact springs added to the tissue model handle the collision between vocal folds.

6. CONCLUSION AND PERSPECTIVES

Our study theoretically compared two existing models of fluid flow in pipes with moving boundaries, from the works of Mora et al. (2021b) and Wetzel (2021). By examining the equivalent electrical circuits derived from these models, we identified structural similarities, particularly the presence of a canonical transmission line structure responsible for the axial dynamics of both models. It appears that when the transverse kinetic energy is neglected, this transmission line is structurally disconnected from the fluid-structure interface. Regarding the connection to deformable fluids, both models use simple lumped parameter representations of tissues as assemblies of springs, dampers, and masses. The key difference lies in the causality of the fluid-structure connection, which is dependent on the presence (or not) of transverse flow dynamics. A method proposed by Mora et al. (2021b) for handling channel closing and based on switch variables, could be applied to both models.

The future trajectory of this research involves several key aspects, including the generalization of Wetzel (2021)'s work through the incorporation of finite-element-like methods with a focus on eliminating constraint equations. Further efforts will be directed towards gaining a comprehensive understanding of fluid-structure interface forces in both models.

ACKNOWLEDGEMENTS

This research was funded, in whole or in part, by l'Agence Nationale de la Recherche (ANR), project ANR-22-CE48-0014. For the purpose of open access, the author has applied a CC-BY public copyright licence to any Author Accepted Manuscript (AAM) version arising from this submission.

	1.a Model of Mora et al. (2021b)	1.b Model of Wetzel (2021)
Geometry	Assembly of rectangular ducts with moving heights	
Energy	Axial kinetic energy Internal energy	Axial kinetic energy Transverse kinetic energy Internal energy
Discretization	Piecewise constant axial velocity Piecewise constant density on a staggered grid	Piecewise linear axial mass flow Piecewise constant density Piecewise linear transverse velocity
Assembled system size	$(3N)$ states	$(5N)$ states $(N-1)$ algebraic constraints
Fluid-structure interface	Velocity controlled	Force controlled
Open boundaries	Enthalpy or mass flow controlled	Enthalpy controlled
State Hamiltonian	$\boldsymbol{x}^m = [\nu_i, \boldsymbol{\nu}^\intercal, \widetilde{\boldsymbol{m}}^\intercal, m_o, \boldsymbol{h}^\intercal]^\intercal$, $H^m(\boldsymbol{x}^m)$ defined by (6)	$\boldsymbol{x}_f = [\boldsymbol{\nu}_l^\intercal, \boldsymbol{\nu}_r^\intercal, \boldsymbol{\pi}_y^\intercal, \boldsymbol{m}^\intercal, \boldsymbol{h}^\intercal]^\intercal$, $H_f(\boldsymbol{x}_f)$ defined by (27)
Equivalent circuit of inner segments	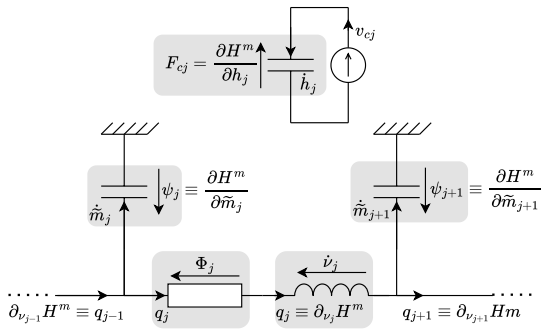	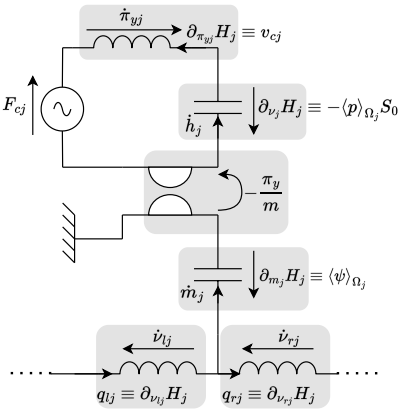

Table 1. Summary of fluid model differences.

REFERENCES

De Vries, M.P., Schutte, H.K., Veldman, A.E.P., and Verkerke, G.J. (2002). Glottal flow through a two-mass model: Comparison of Navier–Stokes solutions with simplified models. *The Journal of the Acoustical Society of America*, 111(4), 1847–1853. doi:10.1121/1.1323716.

Encina, M., Yuz, J., Zanartu, M., and Galindo, G. (2015). Vocal fold modeling through the port-Hamiltonian systems approach. In *2015 IEEE Conference on Control Applications (CCA)*, 1558–1563. IEEE, Sydney, Australia. doi:10.1109/CCA.2015.7320832.

Hélie, T. and Silva, F. (2017). Self-oscillations of a vocal apparatus: a port-Hamiltonian formulation. In F. Nielsen and F. Barbaresco (eds.), *Geometric Science of Information: Third International Conference, GSI 2017, Paris, France, November 7-9, 2017, Proceedings*, 3rd conference on Geometric Science of Information (GSI), 375–383. Springer International Publishing.

Ishizaka, K. and Flanagan, J.L. (1972). Synthesis of Voiced Sounds From a Two-Mass Model of the Vocal Cords. *Bell System Technical Journal*, 51(6), 1233–1268. doi:10.1002/j.1538-7305.1972.tb02651.x.

Lopes, N. and Hélie, T. (2016). Energy Balanced Model of a Jet Interacting With a Brass Player's Lip. *Acta Acustica united with Acustica*, 102(1), 141–154. doi:10.3813/AAA.918931.

Mora, L.A., Le Gorrec, Y., Matignon, D., Ramirez, H., and Yuz, J.I. (2021a). On port-Hamiltonian formulations of 3-dimensional compressible Newtonian fluids. *Physics of Fluids*, 33(11), 117117. doi:10.1063/5.0067784.

Mora, L.A., Ramirez, H., Yuz, J.I., Le Gorec, Y., and Zañartu, M. (2021b). Energy-based fluid–structure model of the vocal folds. *IMA Journal of Mathematical Control and Information*, 38(2), 466–492. doi:10.1093/imamci/dnaa031.

Mora, L.A., Yuz, J.I., Ramirez, H., and Gorrec, Y.L. (2018). A port-Hamiltonian Fluid-Structure Interaction Model for the Vocal folds. *IFAC-PapersOnLine*, 51(3), 62–67. doi:10.1016/j.ifacol.2018.06.016.

Ruty, N., Pelorson, X., Van Hirtum, A., Lopez-Arteaga, I., and Hirschberg, A. (2007). An in vitro setup to test the relevance and the accuracy of low-order vocal folds models. *The Journal of the Acoustical Society of America*, 121(1), 479–490.

Story, B.H. and Titze, I.R. (1994). Voice simulation with a body-cover model of the vocal folds. *The Journal of the Acoustical Society of America*, 97(2), 1249–1260. doi:10.1121/1.412234.

Trenchant, V., Ramirez, H., Le Gorrec, Y., and Kotyczka, P. (2018). Finite differences on staggered grids preserving the port-Hamiltonian structure with application to an acoustic duct. *Journal of Computational Physics*, 373, 673–697. doi:10.1016/j.jcp.2018.06.051.

Wang, X., Zheng, X., Titze, I.R., Palaparthi, A., and Xue, Q. (2023). Examining the Quasi-Steady Airflow Assumption in Irregular Vocal Fold Vibration. *Applied Sciences*, 13(23), 12691. doi:10.3390/app132312691.

Wetzel, V. (2021). *Lumped Power-balanced Modelling and Simulation of the Vocal apparatus : a Fluid-Strucutre Interaction Approach*. Phd thesis, Sorbonne Université.